Internal Flow Field Studies in a Simulated Cylindrical Port Rocket Chamber

R. Dunlap,* A. M. Blackner,† R. C. Waugh,‡ R. S. Brown,§ and P. G. Willoughby¶
United Technologies, San Jose, California 95161

The objective of these studies is to experimentally characterize the mean and fluctuating flow field that develops along the length of a simulated cylindrical port rocket chamber. Flow simulation was accomplished by injecting ambient temperature nitrogen uniformly along the walls of 10.2-cm (4-in.) diam, porous-tube chambers connected to a choked sonic nozzle. Experiments were conducted with chamber L/D ratios of 9.5 and 14.3, at injection Mach numbers and Reynolds numbers typical of rocket motor values. Maximum Reynolds numbers based on injection and centerline velocities were, respectively, 1.8×10^4 and 1.6×10^6. Mean and fluctuating speed and turbulent shear stresses were measured in the principle coordinate directions using three-element hot-wire anemometers. The data show that noticeable velocity fluctuations in the head-end region generally decrease in intensity, relative to centerline speed, over the first five port diameters. At this point, regular velocity oscillations appear near the wall, just prior to the transition to turbulent flow. The oscillation frequency characteristics suggest the occurrence of vortical disturbances which exhibit pairing as they move away from the wall. The downstream turbulence development is characterized by a slow spreading toward the centerline: peak values of turbulence intensity and shear stress occur a few tenths of a port radius from the wall and remain relatively constant. Mean velocity profiles prior to transition show fair agreement with those derived for a rotational inviscid flow injected normal to the surface. A slow transition from these profiles occurs downstream in the turbulent region. Two surprising features of the flow were the occurrence of both buoyant flow influences and flow spinning in forward regions of the chamber.

Introduction

THE internal flow field that develops along the combustion chamber of a solid-propellant rocket motor (SRM) plays a key role in many aspects related to the motor design and operation. Pressure drops required to accelerate the flow along the chamber determine the magnitude and distribution of loads on the propellant, case, and nozzle surfaces. Mean velocity and turbulence characteristics near surfaces determine convective heating loads and therefore affect both insulation thickness requirements and the potential for erosive burning of the propellant. Spatial development of the velocity field determines the growth and trajectories of metal oxide particles and the degree to which they impact, heat, and accumulate on insulated surfaces. The mean velocity and turbulence fields also affect acoustic damping and acoustic interactions with the propellant surface and thereby influence overall motor stability. In this regard, the flow itself can be the driving source for chamber pressure oscillations. This occurs, for example, when flow separations caused by abrupt changes in geometry lead to periodic vortex shedding.

For many years, in the absence of more detailed information, one-dimensional flow analyses were used to model and predict effects of the rocket chamber flow field, and turbulence characteristics were assumed to be similar to those in pipe flow or flat plate boundary layers. In 1966, Culick[1] derived an analytical solution for the steady, incompressible, and inviscid flow field in a cylindrical port rocket chamber, subject to the boundary condition that the fluid entered normal to the burning propellant surface. The velocities in the

axial z and radial r directions, respectively, are given simply by the expressions

$$\frac{u}{u_{\mathfrak{e}}} = \cos\left(\frac{\pi}{2}\frac{r^2}{r_w^2}\right) \tag{1}$$

and

$$\frac{v}{v_w} = \frac{r_w}{r}\sin\left(\frac{\pi}{2}\frac{r^2}{r_w^2}\right) \tag{2}$$

where $u_{\mathfrak{e}}$ is the centerline velocity which increases linearly along the port according to the relation

$$u_{\mathfrak{e}} = \pi\frac{z}{r_w}|v_w| \tag{3}$$

and v_w is the (constant) radial injection velocity at the propellant surface. This flow has the interesting and unique characteristic that while satisfying the inviscid equations of motion, it also satisfies the no-slip boundary condition of a viscous fluid. Noting this, Dunlap et al.[2] showed that this same solution would be expected to closely satisfy the viscous equations of motion since the calculated laminar shear forces acting on a fluid element were typically very small compared to the pressure forces. That is, although the flow represented by Eqs. (1-3) is an exact solution of the inviscid equations of motion, it also essentially satisfies the full viscous equations as well as the appropriate viscous boundary condition and, therefore, may be expected to represent the actual rocket chamber flow field. The relative unimportance of the viscous stresses on the mean flow emphasizes an essential physical difference between the injection-drive flow in a cylindrical port rocket chamber and the flow in a pipe. In a pipe, the velocity profile is determined by a balance between viscous stresses and the pressure gradient; the velocity profile for the injection-driven flow is essentially determined by a balance between inertial forces and the pressure gradient. As will be seen later, even for turbulent flow where Reynolds stresses substantially exceed

laminar shear, the dominant force on the fluid in a cylindrical rocket chamber is still the pressure gradient, although the turbulent shear stress gradient near the surface becomes sufficient to influence the mean flow development.

In order to verify the applicability of Culick's inviscid flow solution, Dunlap et al.[2] conducted the first experiments designed to provide a realistic simulation of the SRM chamber flow field. The apparatus utilized cylindrical porous tubes to provide uniform injection (on a scale characteristic of that for gas evolution from a solid propellant), and the experiments were run at injection Reynolds numbers up to 1.2×10^4, which is typical of rocket motor values. The measured axial velocity profiles showed excellent agreement with Eq. (1).The comparison was made 4.2 diameters from the head end of the chamber at which point the flow exhibited moderate fluctuation levels (between 1 and 2% of centerline speed) across most of the port. Thus, these experiments showed that Culick's inviscid flow solution does indeed represent the actual mean flow field in forward regions of a cylindrical port rocket chamber and that the flow also exhibits some degree of fluctuation within the first 4 diameters.

Numerical studies of the injection driven flow in a cylindrical port were subsequently carried out by Beddini,[3-5] using a parabolic form of the viscous equations of motion together with a second-order closure model for the turbulence. [Reference 5 also contains an excellent review of previous analytical and experimental studies of porous tube and channel flows. Of particular note are the early studies of Taylor,[6] who had derived the same solution for the axial velocity profile in a porous tube that Culick derived independently for the rocket motor problem.Taylor had also noted agreement between Eq. (1) and his porous tube/water flow experiments conducted at maximum injection Reynolds numbers of 7×10^2, which are substantially below rocket motor values.] Beddini's calculations also agreed with Eq. (1) in upstream regions of the flow where the centerline Reynolds number was sufficiently low and the flow was essentially laminar. He also predicted that transition to turbulence would occur when the centerline Reynolds number reached a critical value that was dependent on the injection Reynolds number. Following transition, the velocity profile was predicted to gradually steepen near the wall, as the turbulent shear stresses began to exert an influence on the flow development.

The present studies were undertaken in order to experimentally determine the characteristics of both mean and fluctuating flow field development along the length of a simulated cylindrical port rocket chamber. The injection-driven flow was generated by admitting gaseous nitrogen uniformly along the length of porous tube segments stacked in tandem. A convergent sonic nozzle attached to the chamber aft end assured appropriate boundary conditions in aft regions of the chamber and provided for independent control of injection Mach number and Reynolds number. Both the injection Mach number (0.0018 to 0.0036) and Reynolds number (0.9×10^4 to 1.8×10^4) were typical of rocket motor values. The chamber length-to-diameter ratios (L/D) were chosen to ensure centerline Reynolds numbers would exceed Beddini's[5] estimated critical values so that flow transition would be expected to occur. Emphasis in the measurements was placed on describing the transition from laminar to turbulent flow and characterizing the ensuing development of the turbulence and mean velocity profiles. Use of a three-element hot-wire allowed definition of the three components of turbulence intensity as well as the turbulent shear stresses.

The present data provide new information for the flow structure in the rocket chamber and serve to validate developing numerical computations for the injection-driven chamber flow field. In particular, the turbulence measurements allow for detailed comparisons to be made with a number of different models for the turbulence that have been used successfully in other types of flows. Two surprising features of the flow, in the forward "laminar" region of the chamber, were the occur-

rence of both buoyant flow influences and flow spinning. This further complicates precise modeling of the flow in this relatively simple axisymmetric geometry.

Experimental Apparatus and Instrumentation

The rocket chamber flow field was simulated by controlled gas injection through porous surfaces used to represent the burning propellant. This simulation technique was first used in the early cylindrical port studies where a hot-wire anemometer was employed to determine the velocity field over the wide speed range typically encountered in a rocket chamber.[2] This experimental approach was then developed extensively during cold flow studies carried out in models of the Titan five- and six-segment motors[7] and has since been utilized in a number of studies of the rocket chamber flow field.[8-13]

Apparatus and Test Conditions

The cylindrical port rocket chambers were simulated by butting together either four or six separate segments to produce overall L/D ratios of 9.5 or 14.3. Individual segment construction is illustrated in Fig. 1. Compressed nitrogen enters each segment at four equally spaced circumferential locations, passes through a sonic choke, which ensures equal flow rates in all of the segments, through the flow distribution tube containing 444 equally spaced holes, and finally through the porous bronze cylinder representing the propellant surface. (The porous cylinder has a nominal filtration rating of 5–15 μm and a characteristic spacing between the pores of about 60 μm. Thus, the length scale of nonuniformities in surface injection is typical of that for solid propellants.) A convergent sonic nozzle was connected to the chamber, and the experiments were run at approximately 0.21 MPa (30 psia) to ensure choked flow. Average chamber temperature ranged between $+13$ and $-16°$C during the course of the study.

Both chambers employed the same nozzle to give nominal injection Mach numbers M_w of 0.0027 when $L/D = 9.5$ and 0.0018 when $L/D = 14.3$ at the same aft-end centerline Mach number. In addition, the $L/D = 14.3$ configuration was tested with a larger nozzle which increased M_w to 0.0036. Reynolds number, based on port diameter and aft-end centerline speed, varied in the range of approximately 8×10^5 to 1.6×10^6; corresponding injection Reynolds numbers varied from 9×10^3 to 1.8×10^4. These Reynolds numbers are typical of those for an equal size rocket motor at a chamber pressure of approximately 4.8 MPa (700 psia). The experiments were mostly conducted with the flow centerline horizontal, with the hot-wire probe traversed across the chamber (see Fig. 1) at 30 deg from vertical. A number of tests were also conducted with the flow centerline vertical, to examine potential effects of buoyancy in the head-end region. Further details of the test conditions and procedures are given in Ref. 12.

Instrumentation and Data Reduction

The measurements of mean and fluctuating velocity components used the three-element hot-wire probe illustrated in Fig. 2. The probe was designed by United Technologies' Chemical Systems Division (CSD) and built by Thermo-Systems, Inc. (TSI). The needle supports and wires are arranged to eliminate wake interference over a 30-deg half-angle cone about the z axis. The two hot wires at ± 45 deg to the z axis and in the r-z plane are largely sensitive to axial and radial velocity. The third wire in the z-Θ plane senses tangential velocity. The offset of 1.1 mm (0.044 in.) for the third wire necessitated a spatial correction to the wire voltage to avoid a false indication of tangential velocity in regions of steep axial velocity gradients.

Two probes were calibrated over the Mach number range from 0.00464 to 0.212, at the test pressure of approximately 0.21 MPa (30 psia), in a small wind tunnel. (The second probe was required when a substantial earthquake led to destruction of the first probe after acquiring about 80% of the data.) The wires were connected to three TSI Model 1050 constant tem-
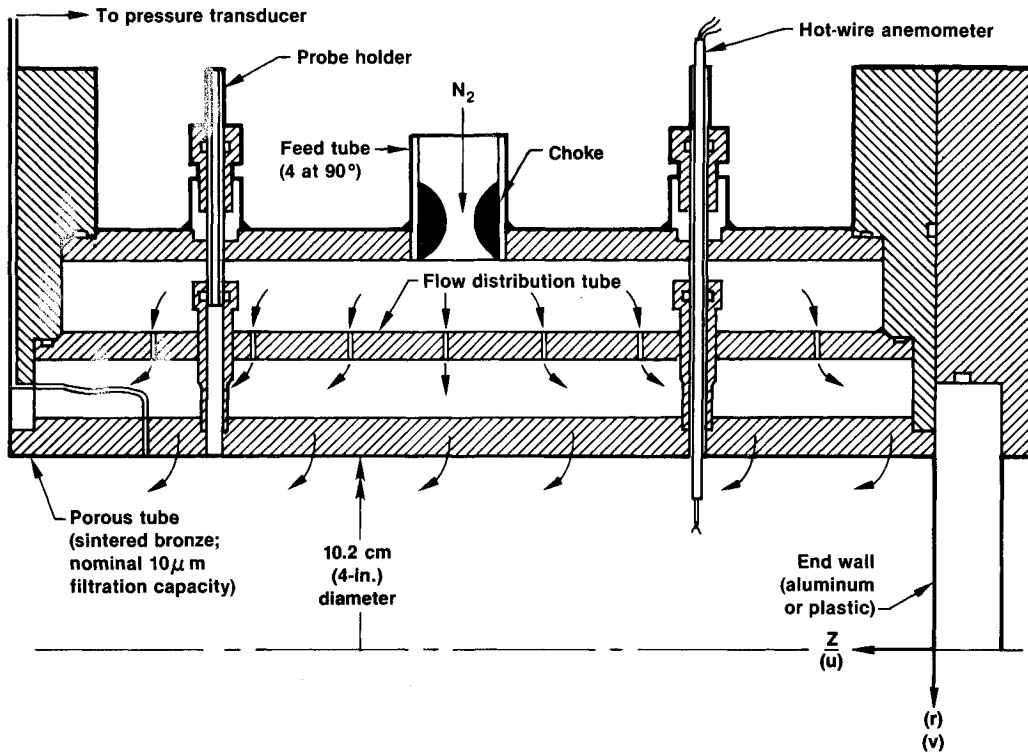
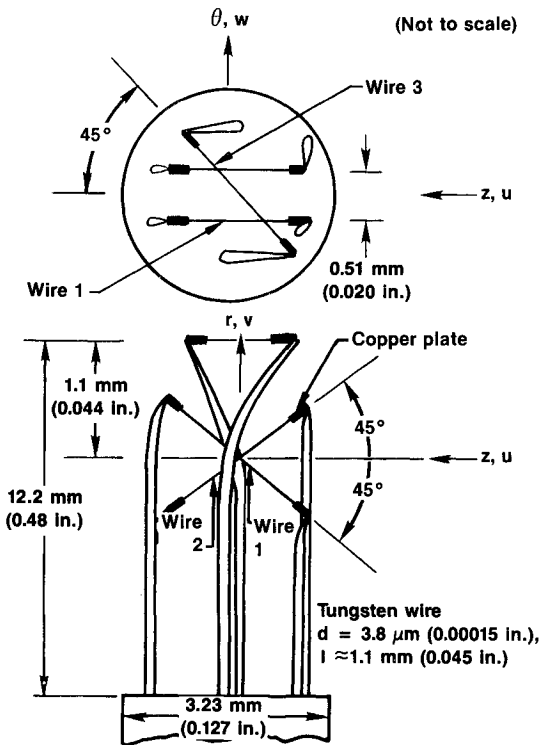Fig. 1   Diagram of cylindrical port segment.

Fig. 2   Schematic drawing of three-element hot-wire probe.

perature anemometers and run at 250°C during both calibration and testing. The probe was pitched and yawed over ± 30 deg to establish angular response characteristics at several test section Mach numbers. A fairly complex analytical fit to the calibration data for each wire was cast in terms of different wire sensitivities to the two perpendicular and the parallel flow components.[12] Maximum expected inaccuracies in predicted flow inclination, owing to residual deviations between the data and analytical fit, were on the order of 2 deg.

Determination of the test flow field mean speeds (u, v, w) in the three coordinate directions (z, r, Θ) involved simultaneous (numerical) solution of the three calibration equations relating each wire mean voltage, pressure, and flow temperature to the velocity components. The assumption of small disturbances was used to form a set of three linear equations relating velocity fluctuations in the three coordinate directions to the three wire voltage fluctuations. The six Reynolds stresses ($\overline{u'^2}$, $\overline{v'^2}$, $\overline{w'^2}$, $\overline{u'v'}$, $\overline{u'w'}$, $\overline{v'w'}$) were then determined as linear functions of the six time-averaged auto- and cross-correlations of the fluctuating wire voltages.

Both mean and fluctuating wire voltages were processed from samples taken through analog-to-digital (A/D) converters with a Data General Nova III computer. At least 1000 samples of each signal were obtained, either on line or by playback of the signal recorded with a Bell and Howell Model 270 FM tape recorder. To obtain spectral and length-scale information, the tape record was played directly into a Hewlett-Packard digital signal analyzer, Model 5420A.

A check was made to determine whether any probe/flow interference effects may exist that are not accommodated by the probe calibration. This was accomplished by taking data in a fully developed pipe flow and then comparing it with the data of Laufer.[14] The comparative results generally show good agreement and suggest no major probe interference effects on the turbulence and mean flow measurements for locations greater than 0.1 to 0.2 port radii from the walls.[12] Furthermore, subsequent comparisons between the three-element hot wire and a much smaller split film probe generally showed very good agreement for wall locations as close as 0.05 port radii in an injection-driven flow similar to that in the present study.[12]

Results and Discussion

Buoyancy Considerations

During the course of early testing, there were a number of indications of flow asymmetry that appeared to be associated with head-end/flow temperature differences. [This temperature difference occurs naturally since the entering flow is generally much cooler than the hardware due to expansion

from the 14 MPa (2000 psi) storage tanks. Thus, since the gases pass through the porous surfaces, these surfaces cool more quickly than the head-end wall.] Though the asymmetries were not generally repeatable (probably due to changes in relative initial hardware and gas temperatures), they suggested that buoyant effects may have some influence on the flow development. The possibility of buoyant effects in the head-end region is not unreasonable in view of the low speeds. For example, the pressure change due to gravity in 5.1 cm (2 in.) is about 2.6 times the pressure change due to radial flow deceleration when $M_w = 0.0018$. Thus, a 5% difference in temperature between the head-end wall and the flow (maximum observed in these tests) would produce a buoyant pressure unbalance equal to 13% of the flow pressure change when the centerline of the experiment is horizontal. This unbalance could cause a noticeable deflection of horizontal steamlines near the head-end and possibly induce recirculating flows.

In general, the ratio of buoyant pressure unbalance to flow pressure change may be expressed by the dimensionless group

$$\frac{\Delta P_{\text{BUOYANCY}}}{\Delta P_{\text{FLOW}}} = \frac{g\ell}{M^2 a^2} \frac{\Delta T}{T} \qquad (4)$$

where ℓ is a characteristic length, g is gravitational acceleration, a is sound speed, and ΔT is the difference between wall and flow temperature. (This ratio is also equal to the Grashof number divided by the square of the Reynolds number.[15]) Choosing $\ell = D$, $M = M_w = 0.0018$, and $\Delta T/T = 0.05$, gives the ratio of 0.13 noted previously for the present tests at maximum observed ΔT. It is of interest to note that the pressure ratio could be considerably larger in a rocket motor. Whereas a^2 is about 10 times greater in the rocket chamber, $|\Delta T|/T$ varies from nearly unity at ignition to typical steady-state values on the order of 0.20. Thus, in a 41-cm (16-in.) diam motor the buoyant pressure change would essentially equal the flow pressure change at ignition and remain at 20% of the flow value during steady-state operation. Increasing scale, or g loading due to acceleration, results in proportionately greater effects.

To minimize potential buoyant effects in the present experiments, the hardware was cooled 1–2 min prior to data sampling. This helped but did not eliminate the wall/flow temperature difference, which varied from a few degrees centigrade to as much as 15°C. Although most of the data were taken with the flow centerline horizontal, the experiment was finally turned vertical to check for differences in the flow field at several head-end stations, as discussed next.

Flow Field Measurements in the L/D = 9.5 Configuration

The distributions of mean axial, radial, and tangential velocity at the most upstream station (i.e., $Z/D = 0.62$) are shown in Fig. 3 for both horizontal and vertical flows. For comparison, the analytical solution derived by Culick[1] is also shown. In this solution, the dimensionless ratio $2\pi Z/D$ (v/u_{ℓ}) is the ratio of radial velocity to injection velocity. The measured axial velocity profile shows a dip in the center which may reflect flow retardation in the end-wall boundary layer. A corresponding increase relative to the cosine variation occurs in the outer flow regions. There may be a small average difference, on the bottom-dead-center (BDC) side, of the profile shape between the horizontal and vertical flows. The radial velocity shows fair agreement with the predicted variation, again with a small average difference between horizontal and vertical orientations. A surprising result was the swirling flow close to the centerline that is clearly evident in the vertical position. In the horizontal position, the swirl pattern appears noticeably different, especially at the two higher wall-minus-flow temperature differences. [The data point at $r/r_w = 0.75$ (TDC) at $T_{\text{wall}} - T_{\text{flow}} = 8.0°C$ showed a substantial flow change but was outside the angular range of the probe calibration.] This may reflect circumferential flow recirculations driven by buoyancy.

Turbulent intensity distributions in the three coordinate directions are shown in Fig. 4 for $Z/D = 0.62$. The distributions are relatively symmetrical with a substantial peak near the centerline, especially in v' and w'. As with the mean speeds, differences between horizontal and vertical flow are most noticeable in the circumferential component where they generally correlate with wall-minus-flow temperature difference.

Spinning of the core region vertical flow is still apparent at $Z/D = 1.8$ and 3.04 (see Fig. 5). Although data for horizontal flow at $Z/D = 1.8$ was not taken in this configuration, the $Z/D = 3.04$ data for horizontal flow shows a significant difference when compared to the vertical flow. It appears that possible buoyant effects in the head-end persist a significant distance downstream.

A schematic illustration of the centerline flow spin development is shown in Fig. 6. Whether the occurrence of spin represents a more naturally stable coalescence of the radially directed stream tubes (given any slight geometric asymmetry) or simply a small angular offset of flow at the porous surface is open to question. The porous tubes are quite concentric, the diameter typically not varying more than 0.25 mm (0.010 in.) around the circumference. Presumably angular offsets normal

Symbol	$T_{\text{wall}} - T_{\text{flow}}$ (C)
O	3.4
◇	6.8
□	8.0

Symbol	Flow Configuration
●	Vertical
O ◇ □ (open)	Horizontal

Note:
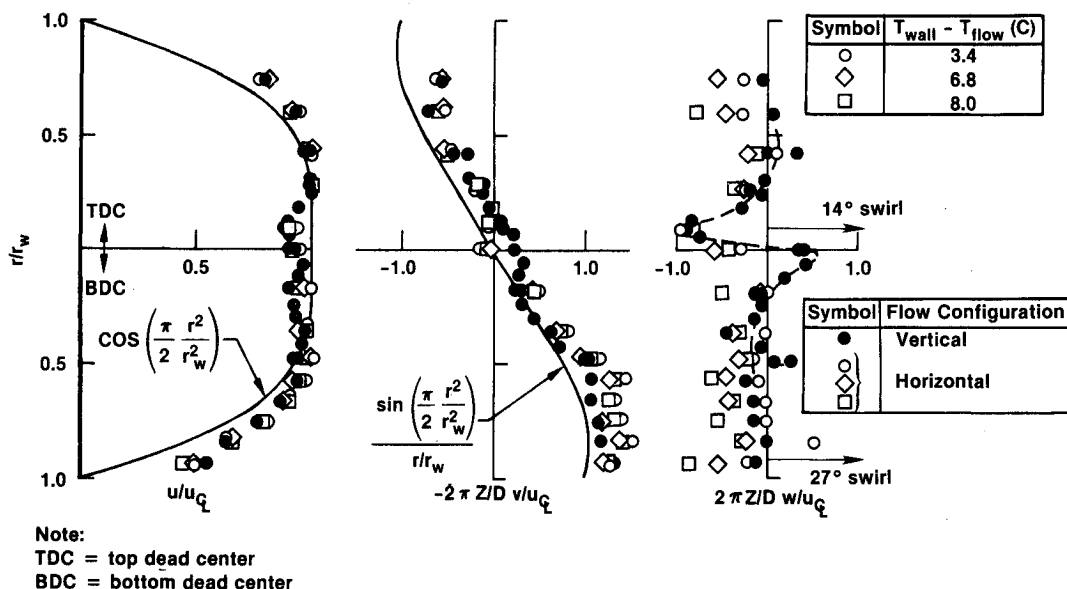TDC = top dead center
BDC = bottom dead center

Fig. 3 Axial, radial, and circumferential velocity profiles at $Z/D = 0.62$.
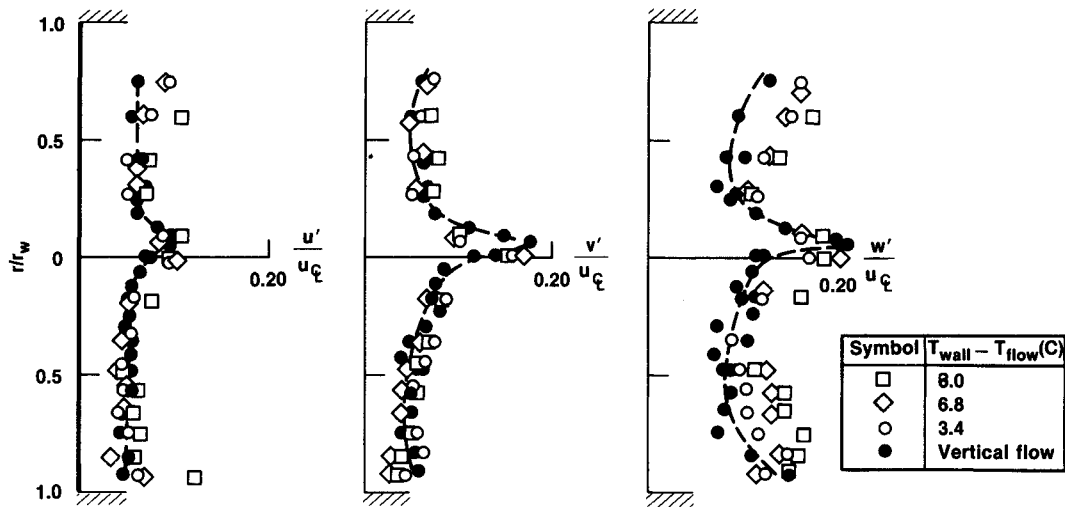
Fig. 4   Comparison of turbulent intensity profiles for horizontal and vertical experiments at Z/D = 0.62.
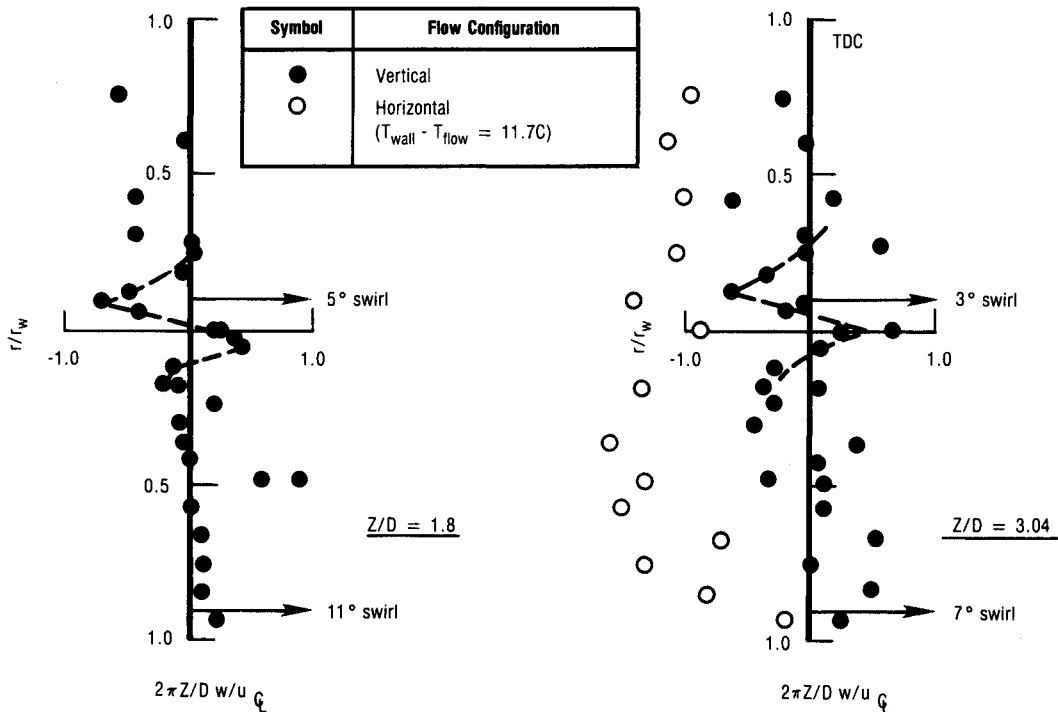

Fig. 5   Circumferential velocity profiles at Z/D = 1.8 and 3.04 (L/D = 9.5, M_w = 0.0027).

to the surface should be random. There is some indication of counterswirl in the outer regions, especially in Fig. 3. With a single traverse of the flow, it is not possible to estimate the net flow rotation.

Development of the axial velocity profile along the length of the port is shown in Fig. 7. At Z/D = 1.8 and 3.04, the velocity agrees quite well with the cosine distribution. The profile at Z/D = 3.04 is noticeably more symmetric when the flow is vertical. Comparisons with vertical flow have not been made at Z/D = 5.46 and 7.88; however, the asymmetry in horizontal flow at Z/D = 3.04 is also evident at these stations. No substantial deviations from the cosine distribution have occurred up to Z/D = 7.88. The variation of centerline Mach number with axial position closely followed the expected linear variation, [see Eq. (3)]; the data are presented subsequently in Fig. 21 together with the results for the L/D = 14.3 configuration.

The turbulence intensity and shear stress distributions (see Figs. 8–11) have undergone a significant change between $Z/$

D = 5.46 and 7.88, where transition to turbulent flow has occurred. The strong centerline peak in turbulence at Z/D = 0.62 is substantially reduced at Z/D = 1.8, and intensity peaks appear in the middle region of the flow at Z/D = 1.8 and 3.04. At Z/D = 5.46, a small peak appears in the near-wall region at BCD. As will be shown, natural oscillations preceding transition occur in this region. The flow is asymmetric at Z/D = 5.46, with transition appearing to start sooner near TDC. In Fig. 11, the maximum shear stress levels have been shown. At Z/D = 1.8, this was the circumferential stress $\overline{v'w'}$, whereas the axial stress $\overline{u'v'}$ is dominant downstream. The peak shear stress at Z/D = 7.88 is about twice the value that would occur at the wall in a fully developed pipe flow at the same Reynolds number.

The axial velocity fluctuations at Z/D = 5.46 are replotted in Fig. 12 together with spectra of the wire voltage oscillations for the three points closest to the wall. At r/r_w = 0.75, almost all of the power is concentrated in a relatively narrow frequency band centered about 230 Hz. (Spectra at r/r_w = 0.66

and 0.57 are similar, but the peak is less intense relative to the background.) The leading edge of this frequency band is close to the first longitudinal acoustic mode of 180 Hz. Closer to the wall, a second peak begins to occur at about twice the frequency of the outer peak. This frequency doubling is more dramatically illustrated at the same axial and radial positions in the L/D = 14.3 configuration when M_w = 0.0018, as shown in Fig. 13. In this case, the nominal aft-end centerline speed is the same as for the L/D = 9.5 configuration, but the local velocities at the same Z/D have decreased inversely with L/D. The frequencies involved have dropped almost exactly in proportion to the change in local mean flow velocity and also in proportion to the change in acoustic mode frequency.

Examination of the spectra in Fig. 14 for L/D = 14.3 and M_w = 0.0036 shows a similar behavior as when M_w = 0.0018, but the center frequencies have doubled to 280 Hz at r/r_w = 0.75 and 590 Hz at r/r_w = 0.93. Thus, the oscillation frequency scales with local flow speed rather than a fixed acoustic mode value. The frequency halving, as distance from the wall is increased, is suggestive of vortical disturbances, which exhibit vortex pairing as illustrated in Fig. 15. An upstream vortical disturbance originating close to the wall overtakes a neighboring downstream disturbance since it is convected at higher relative speed. As described by Winant and Browand,[16] in the pairing process, the size doubles and the frequency therefore is halved. The scaling of frequency with flow speed implies vortical sizes are also independent of flow speed.

Flow Field Measurements in the L/D = 14.3 Configuration

The L/D = 14.3 configuration just introduced was actually tested first (only in the horizontal position). During the course of these measurements, a small mass flow disturbance, where
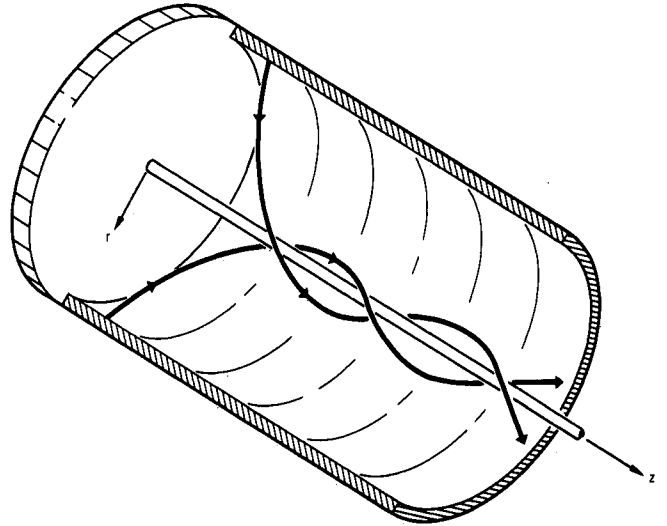
Fig. 6   Schematic diagram of spinning flow.
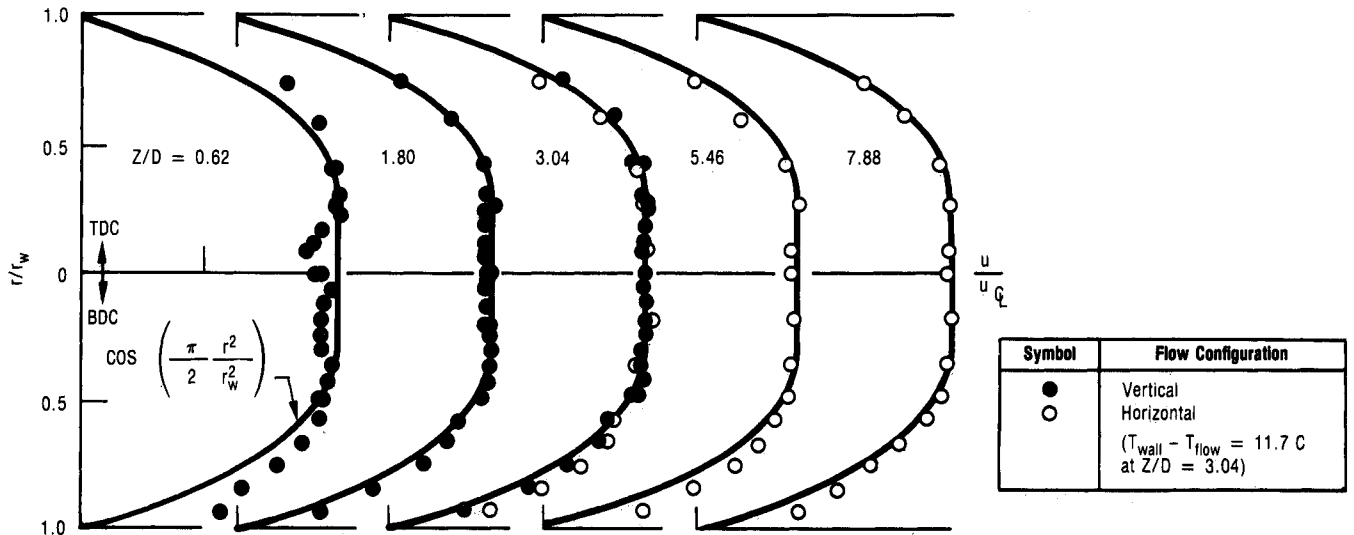
Fig. 7   Development of axial velocity profiles in cylindrical port (L/D = 9.5, M_w = 0.0027).
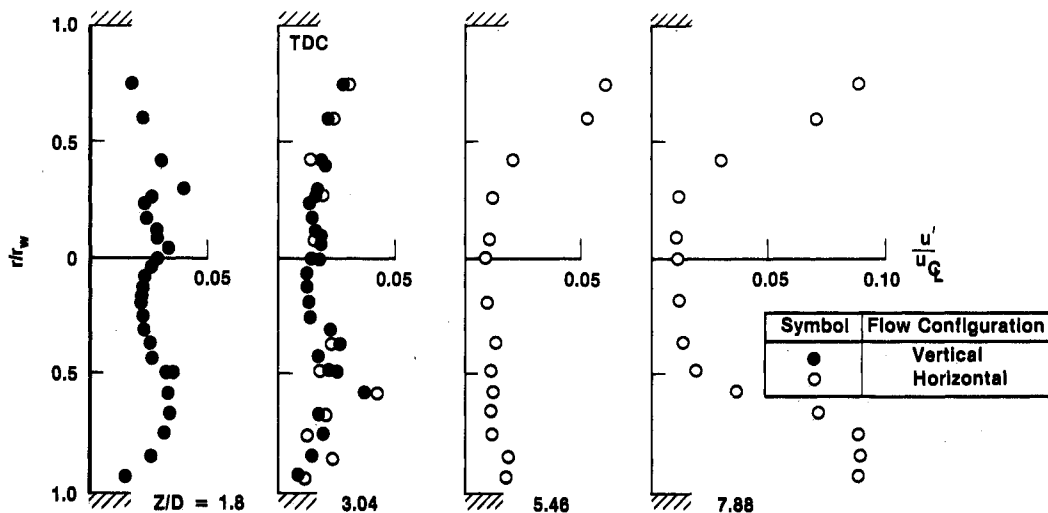
Fig. 8   Distribution of longitudinal turbulent intensity in cylindrical port (L/D = 9.5, M_w = 0.0027).
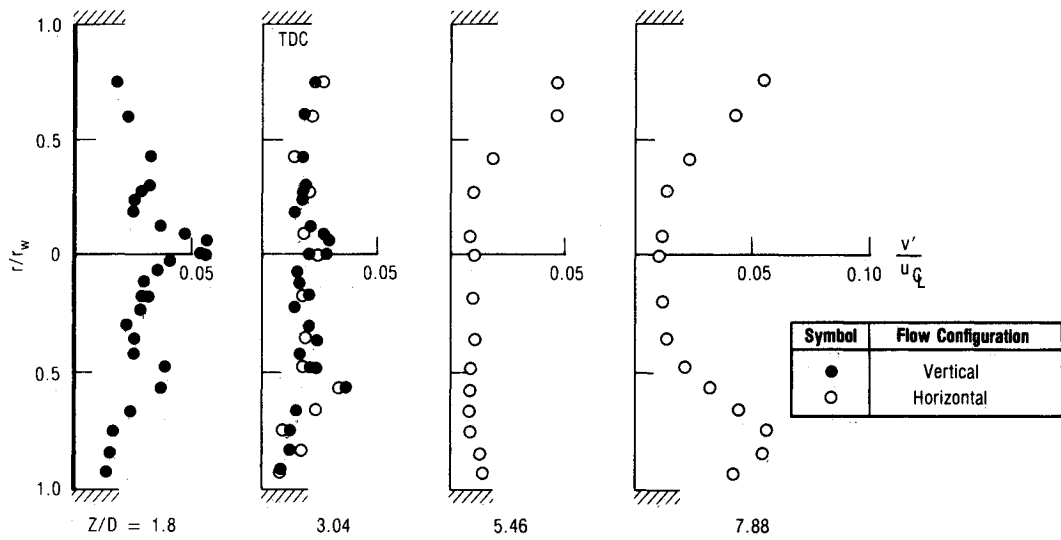
Fig. 9   Distribution of radial turbulent intensity along cylindrical port ($L/D = 9.5$, $M_w = 0.0027$).
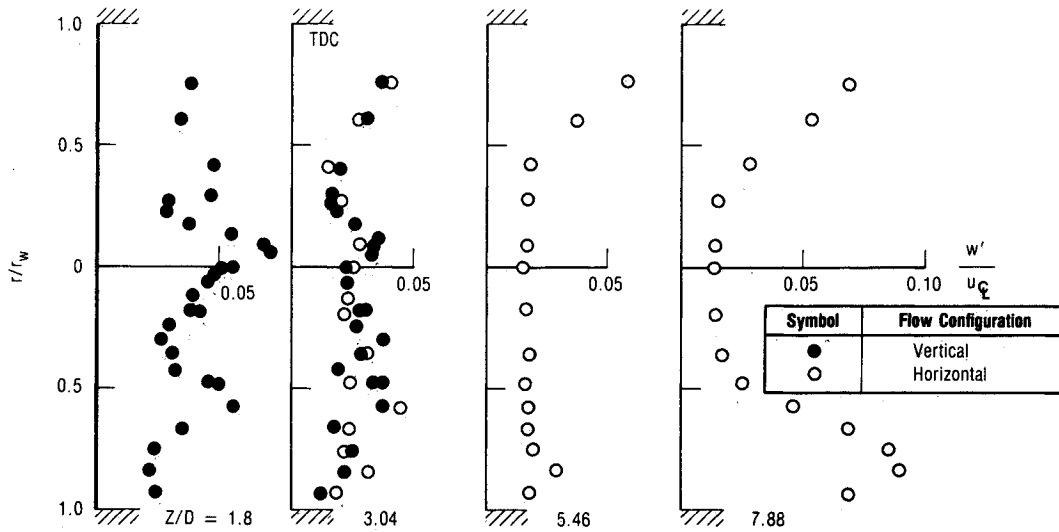

Fig. 10   Distribution of circumferential turbulent intensity along cylindrical port ($L/D = 9.5$, $M_w = 0.0027$).
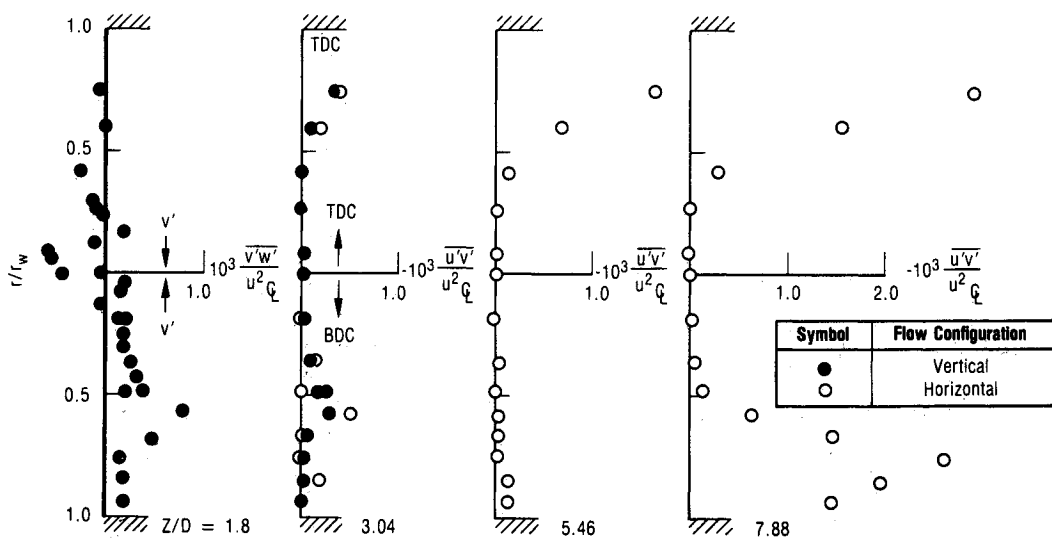

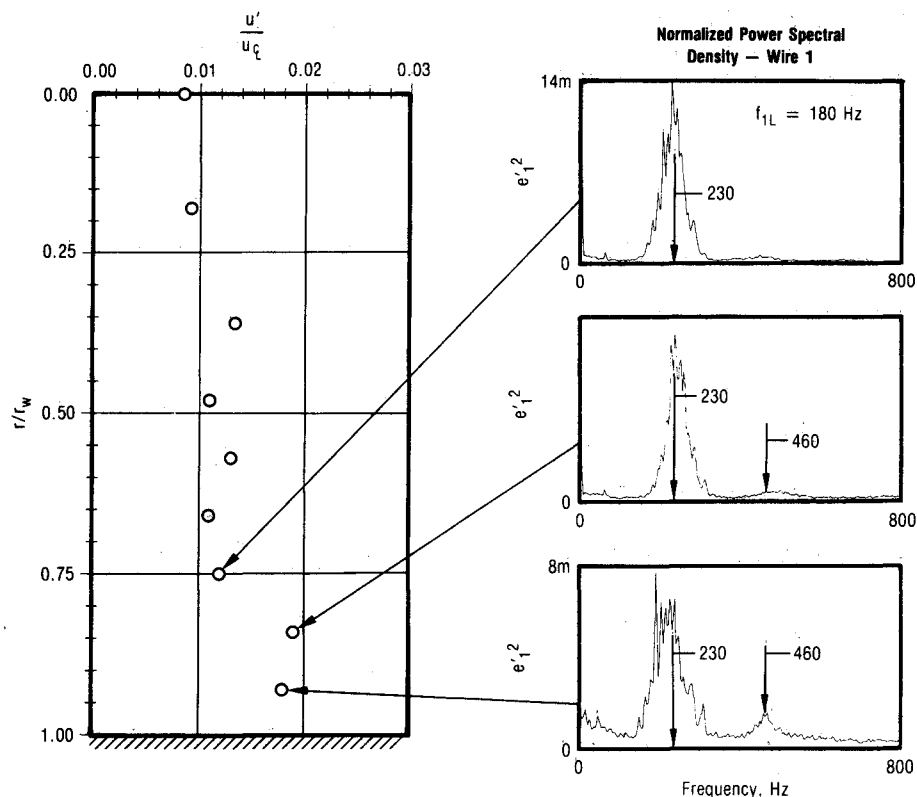Fig. 11   Distribution of turbulent shear stress along cylindrical port ($L/D = 9.5$, $M_w = 0.0027$).

Fig. 12   Natural oscillations in cylindrical port at $Z/D = 5.46$ ($L/D = 9.5$, $M_w = 0.0027$).
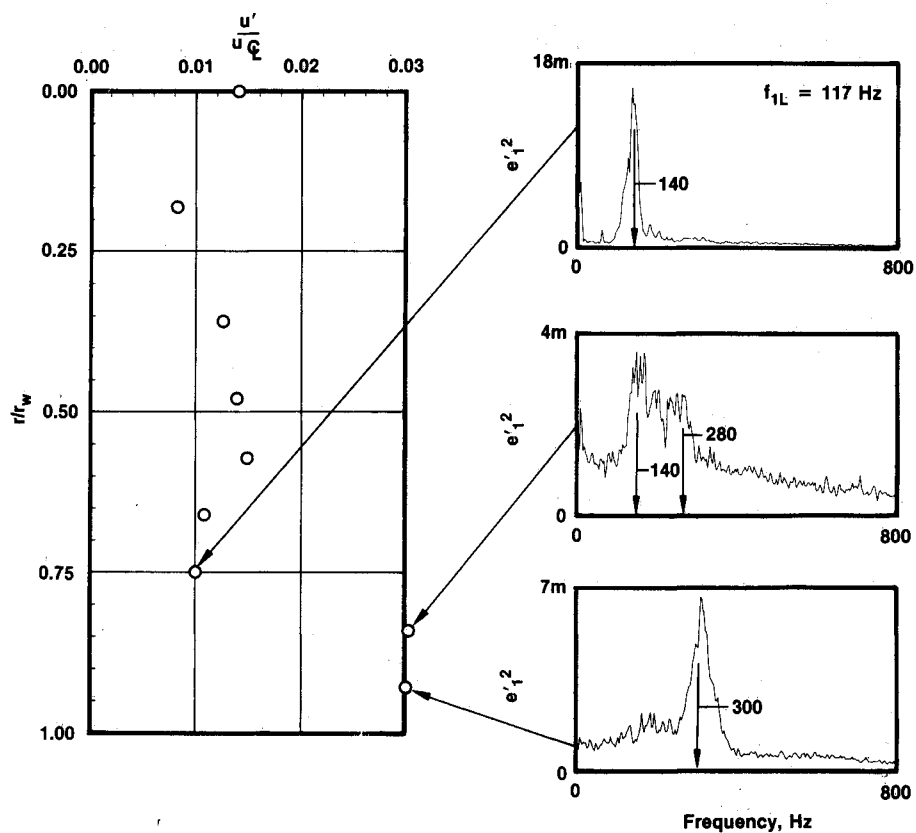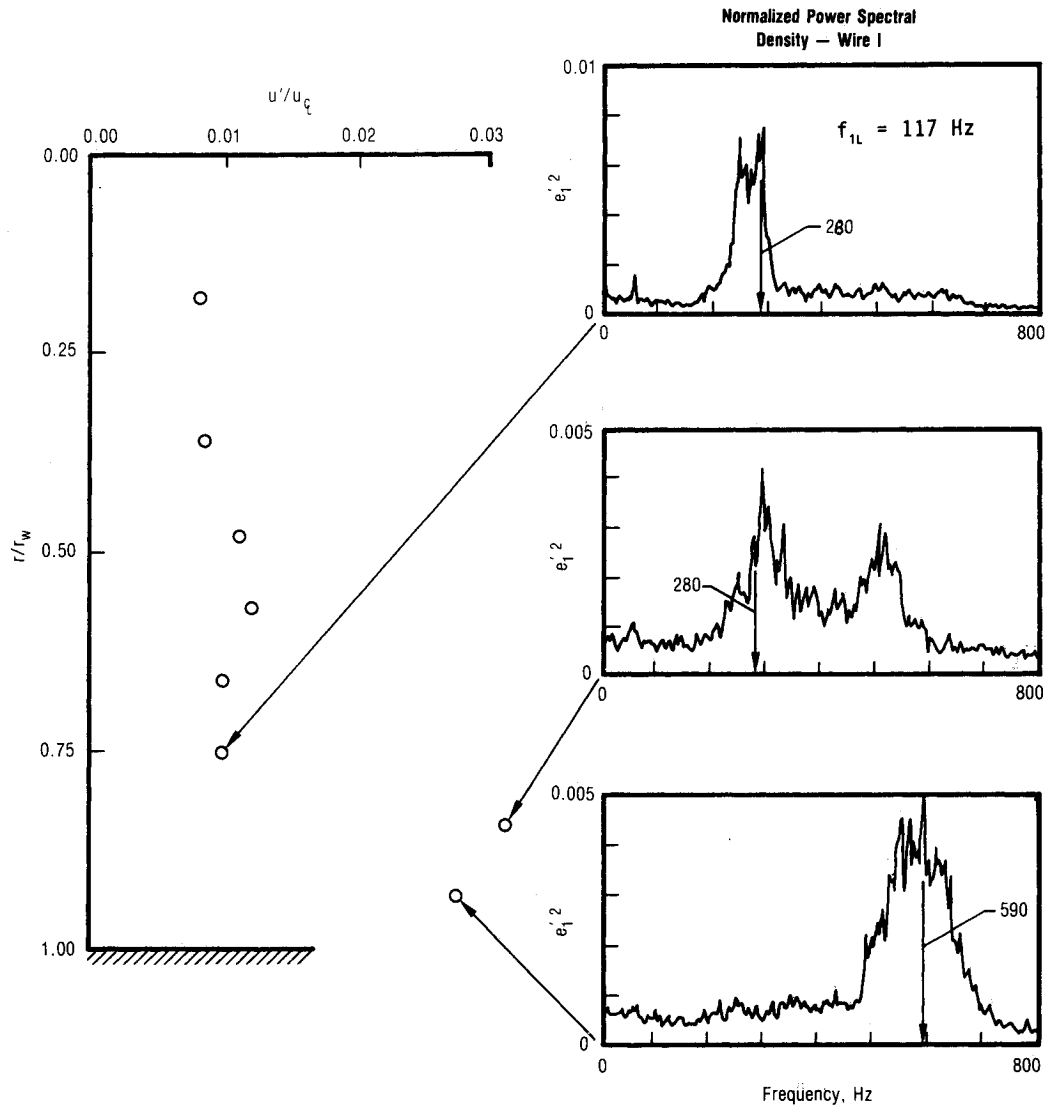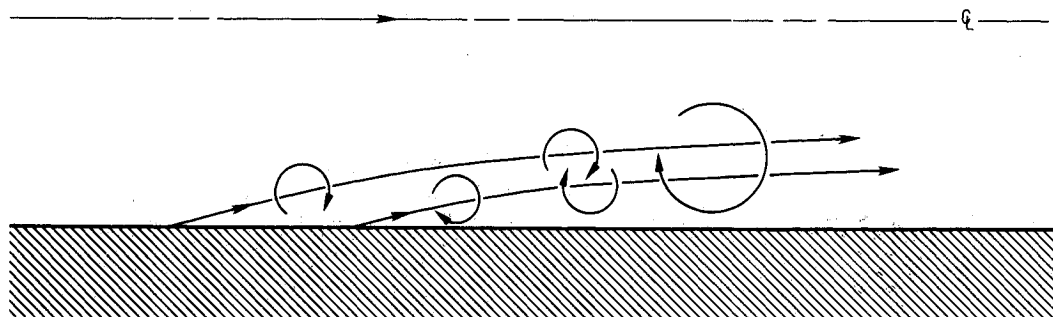

Fig. 13   Natural oscillations in cylindrical port at $Z/D = 5.46$ ($L/D = 14.3$, $M_w = 0.0018$).

Fig. 14 Natural oscillations in cylindrical port at $Z/D = 5.46$ ($L/D = 14.3$, $M_w = 0.0036$).

Fig. 15 Vortex pairing as potential mechanism for frequency halving of natural oscillations in cylindrical port flow.

the hot-wire probe entered the port at TDC, was found to produce noticeable effects in a portion of the upstream flow regions on the TDC side of the port. This disturbance was eliminated in the $L/D = 9.5$ data just shown, and its influence on the data was also examined in the $L/D = 9.5$ configuration by comparing measurements before and after eliminating the disturbance.[12] The disturbance was confined to the TDC side of the port and did not influence the measurements beyond 3 port diameters. Data which may have been influenced by the disturbance in the $L/D = 14.3$ configuration are omitted in the following figures.

Radial profiles of the normalized axial, radial, and circumferential rms turbulent fluctuations are shown from $Z/D = 0.62$ to 12.72 in Figs. 16-18. As just shown (Figs. 13 and 14), natural oscillations occur near BDC when Z/D is 5.46. As with the $L/D = 9.5$ configuration, these oscillations are the precursor to transition, which begins near TDC at $Z/D = 5.46$ and results in fairly symmetric turbulence profiles by $Z/D = 7.88$. For Z/D greater than 7.88, the profiles remain fairly symmetric with peak values close to the wall remaining relatively constant at about 0.07 to 0.08 for u'/u_t, 0.04 to 0.05 for v'/u_t, and 0.06 to 0.08 for w'/u_t. These values are
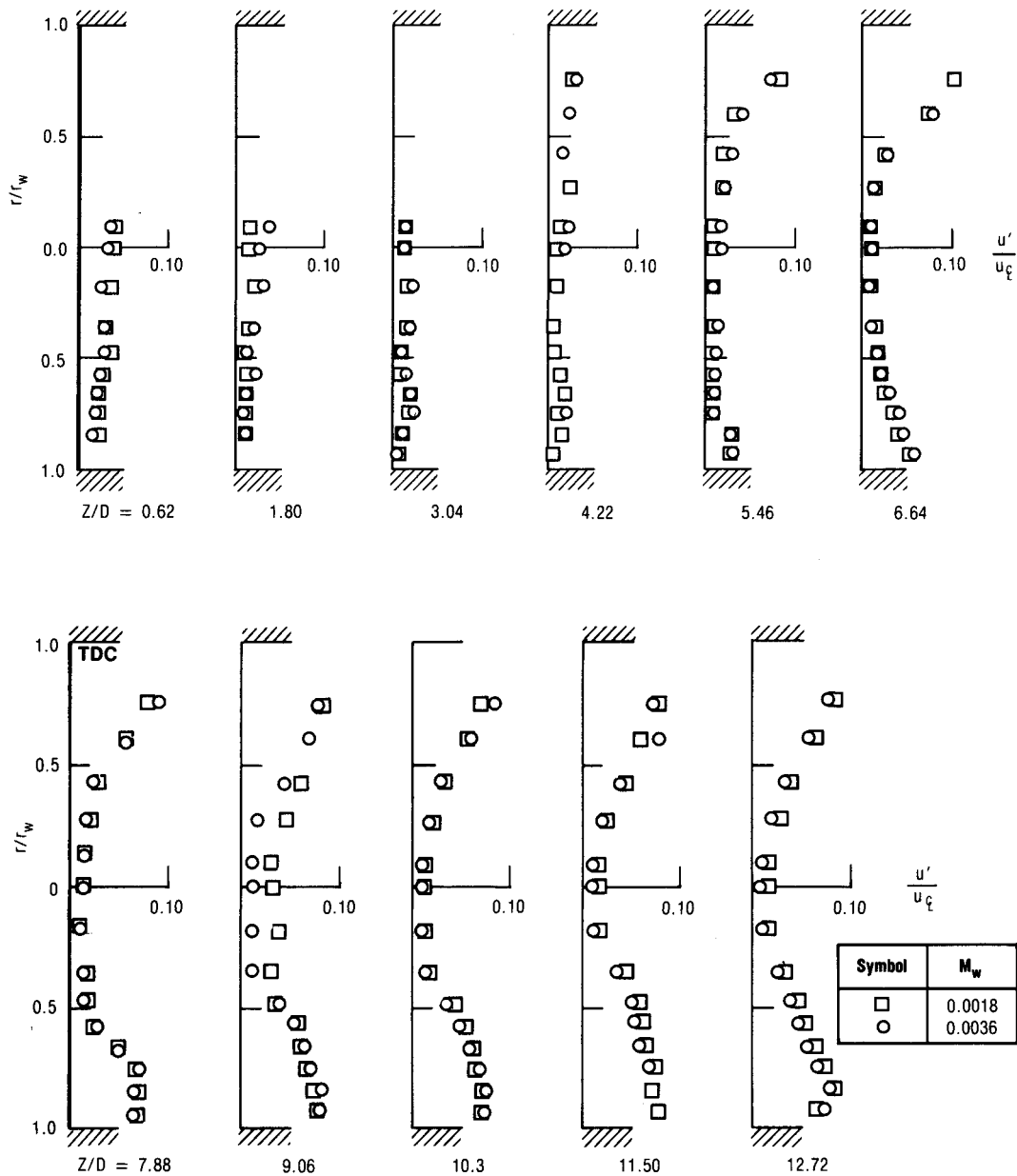
Fig. 16   Distribution of longitudinal turbulent intensity along cylindrical port ($L/D = 14.3$).

similar to peak values measured by Laufer[14] near the wall at $Re_D = 5 \times 10^5$ for fully developed pipe flow, although the present values of v' and w' are generally a greater fraction of u' than in pipe flow. The turbulence profiles are seen to gradually bloom out toward the centerline with increasing length. The centerline turbulent intensities remain unchanged at about 1 to 2% of the local centerline velocity. The turbulent shear stress profiles (see Fig. 19) show an axial variation similar to the turbulent intensities. (The "non-smooth" variation with the radius of some of the $u'v'$ data is believed to reflect fairly high levels of unsteadiness in $u'v'$ itself, as was determined in some later experiments involving a somewhat different geometry.[12] The reason for the unusual variation in $u'v'$ at $Z/D = 11.50$ and $M_w = 0.0018$ is unknown; however, it is suggestive of a slippage of the probe where it attaches to the traverse.) In the turbulent region, peak values are from 60 to 100% greater than those near the wall in a pipe flow (at the same centerline velocity) where shear stress increases linearly from the centerline to the wall. The present data indicate little effect of the injection or centerline Reynolds number on the location of transition and the ensuing turbulence development.

As noted in the introduction and discussed in Ref. 2, a major difference between the injection-driven flow in a cylindrical port and pipe flow is the importance of axial shear forces relative to pressure gradient forces. These forces are in balance in a fully developed pipe flow. For the laminar injection-driven flow, the axial force due to the shear stress was shown to be negligible compared to the pressure gradient forces. For the present injection-driven flow, in the downstream regions of measurement where the dominant shear stresses are typically the turbulent Reynolds stresses, the ratio of net pressure to shear force acting on a fluid element is given closely by

$$R = \frac{\text{pressure force}}{\text{shear force}} \approx \frac{\dfrac{-2}{\rho u_\ell^2} \dfrac{\partial P}{\partial(z/r_w)}}{2 \dfrac{\partial(-u'v'/u_\ell^2)}{\partial(r/r_w)}} \qquad (5)$$

The measured values of normalized pressure gradient,

$$\frac{-2}{\rho u_\ell^2} \frac{\partial P}{\partial(z/r_w)} = \frac{2}{M_\ell} \frac{dM_\ell}{d(z/r_w)} \qquad (6)$$
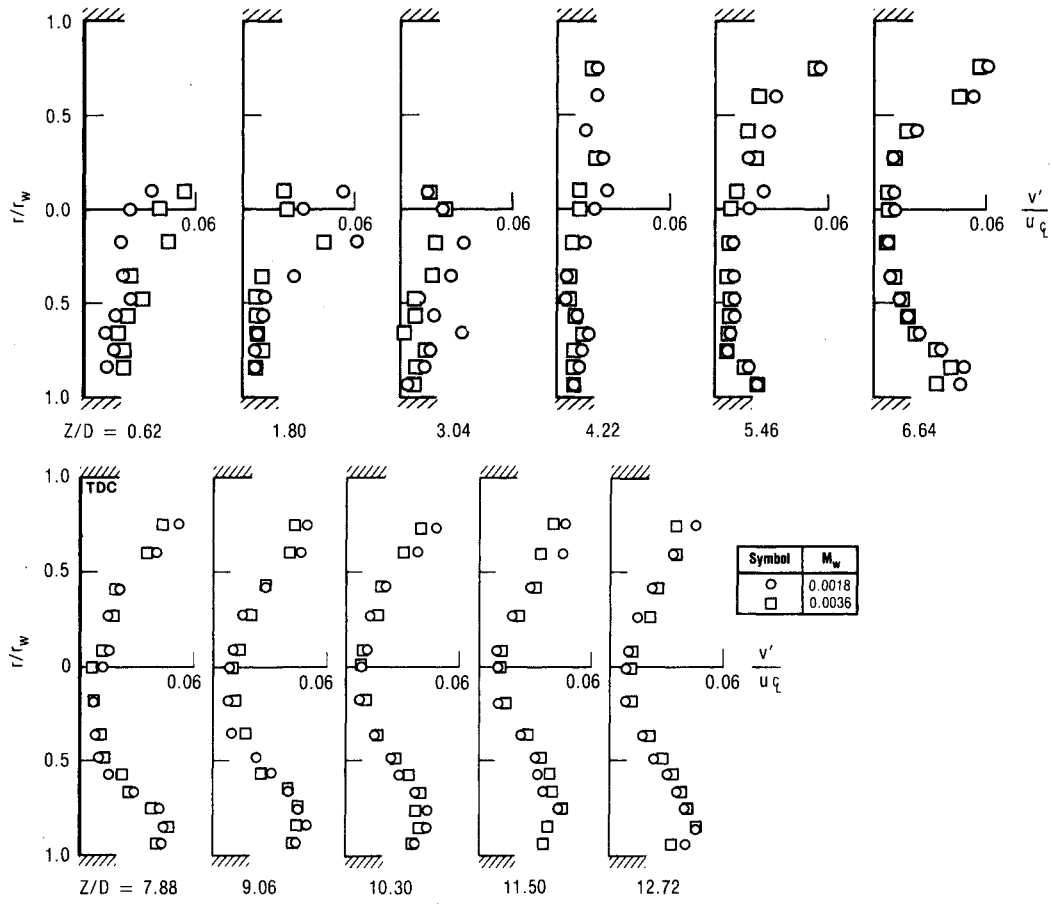
Fig. 17   Distribution of radial turbulent intensity along cylindrical port (L/D = 14.3).
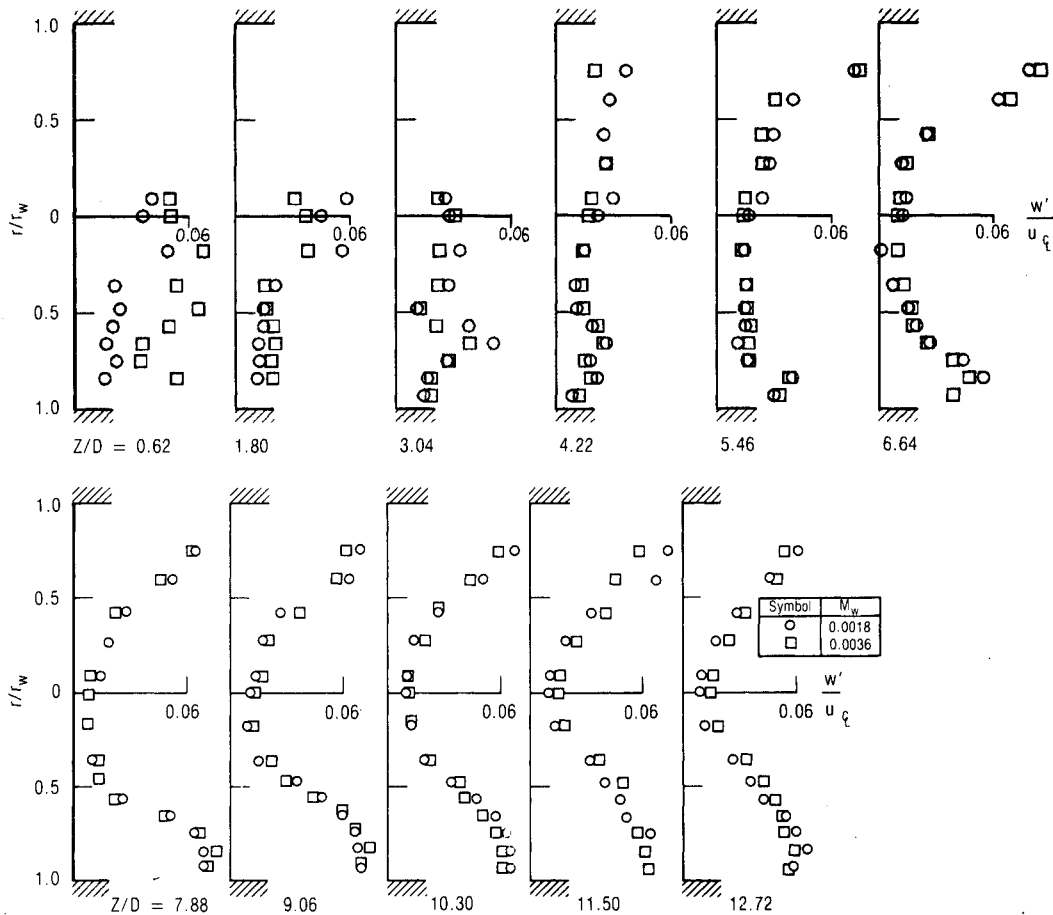

Fig. 18   Distribution of circumferential turbulent intensity along cylindrical port (L/D = 14.3).
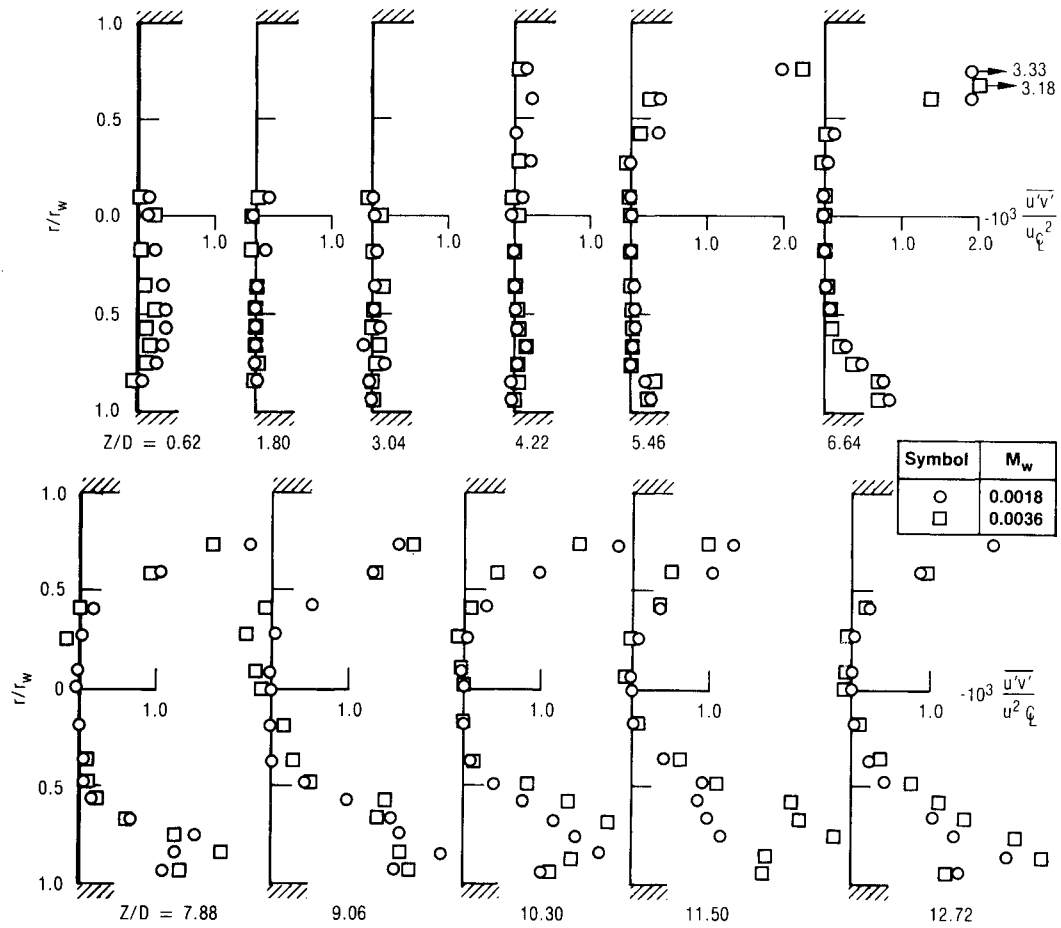
Fig. 19   Distribution of turbulent shear stress along cylindrical port ($L/D = 14.3$).
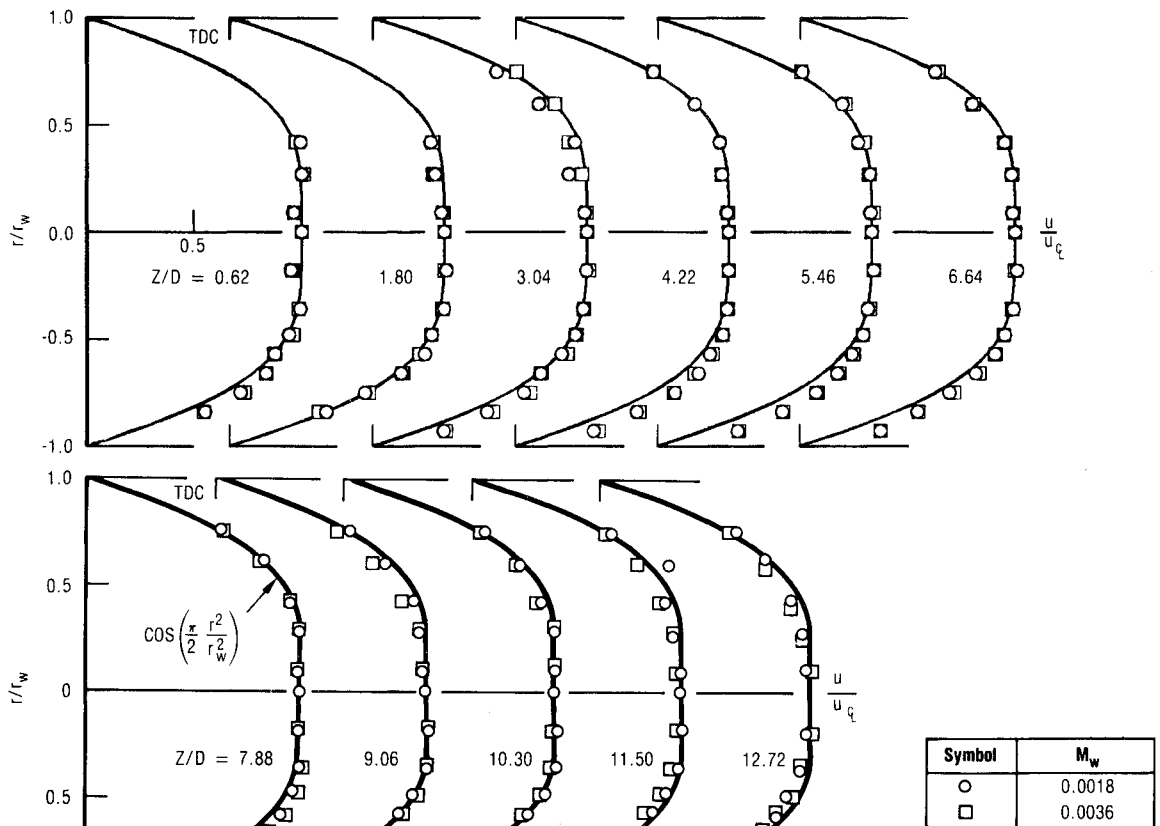

Fig. 20   Development of axial velocity profiles along cylindrical port ($L/D = 14.3$).

had values close to those calculated from the analytical solution of Culick[1] where $(2/M_t)dM_t/d(z/r_w) = (z/D)^{-1}$. Thus,

$$R \approx \left[2 \frac{z}{D} \frac{\partial(-\overline{u'v'}/u_t^2)}{\partial(r/r_w)} \right]^{-1} \qquad (7)$$

Between the centerline and the peak in $\overline{u'v'}$, where the shear stress acts to retard the flow, $|\partial(-\overline{u'v'}/u_t^2)/\partial(r/r_w)|$ is typically less than about 4×10^{-3}, and $|R|$ is greater than 10. Thus, the pressure forces remain the dominant force acting on the majority of the fluid in the turbulent case as well as in the laminar, at least for L/D ratios of practical interest. In regions closer to the wall, where the shear stress acts to accelerate the flow, it exerts a greater influence; however it still appears to exert less than half the influence of the axial pressure gradient.

The development of axial velocity profiles is compared with the cosine variation in Fig. 20. Upstream of transition, the profiles generally agree quite well with the expected cosine variation. In the downstream turbulent region the closest wall point remains at a nearly constant fraction of centerline speed (about twice the cosine profile value). There is a gradual decrease in normalized velocity midway between the wall and the centerline as a result of the net shear stress on the fluid. The very gradual change in profile shape is consistent with the relatively low shear stress levels in comparison to pressure gradients. The variation of centerline Mach number with axial position is shown in Fig. 21 together with the $L/D = 9.5$

results. The Mach number follows the linear analytical variation (to within a few percent) prior to transition and then increases a little more slowly in the turbulent region.

A final set of measurements were made in a turbulent pipe flow with the objectives of both checking the present measurement technique against Laufer's data[14] and also determining a turbulent length scale for comparison with the injection driven flow. The experiment used a 10.2-cm (4-in.) diam plastic pipe, 6.1-m (20-ft) long, and employed the same hot-wire probe used in the porous tube studies. These experiments were undertaken in view of initial comparisons between the present data and CFD calculations by Beddini[12] and by Sabnis et al.[17] Both predictions, which employed different turbulence models, yielded shear stress values typically twice those measured in the downstream turbulent regions of the injection-driven flow. Thus, it was desirable to first insure that there were no unforeseen problems with the present measurement techniques. As discussed earlier (see instrumentation description), generally good agreement was in fact found between the present measurements and those of Laufer.

Since the prediction techniques worked well in turbulent pipe flow, it was suggested that the overprediction for the injection-driven flow may reflect turbulent length scale differences not accounted for in the model predictions. The experimental turbulent length scale comparison was made for the integral scale defined here as $u\tau_E$, where

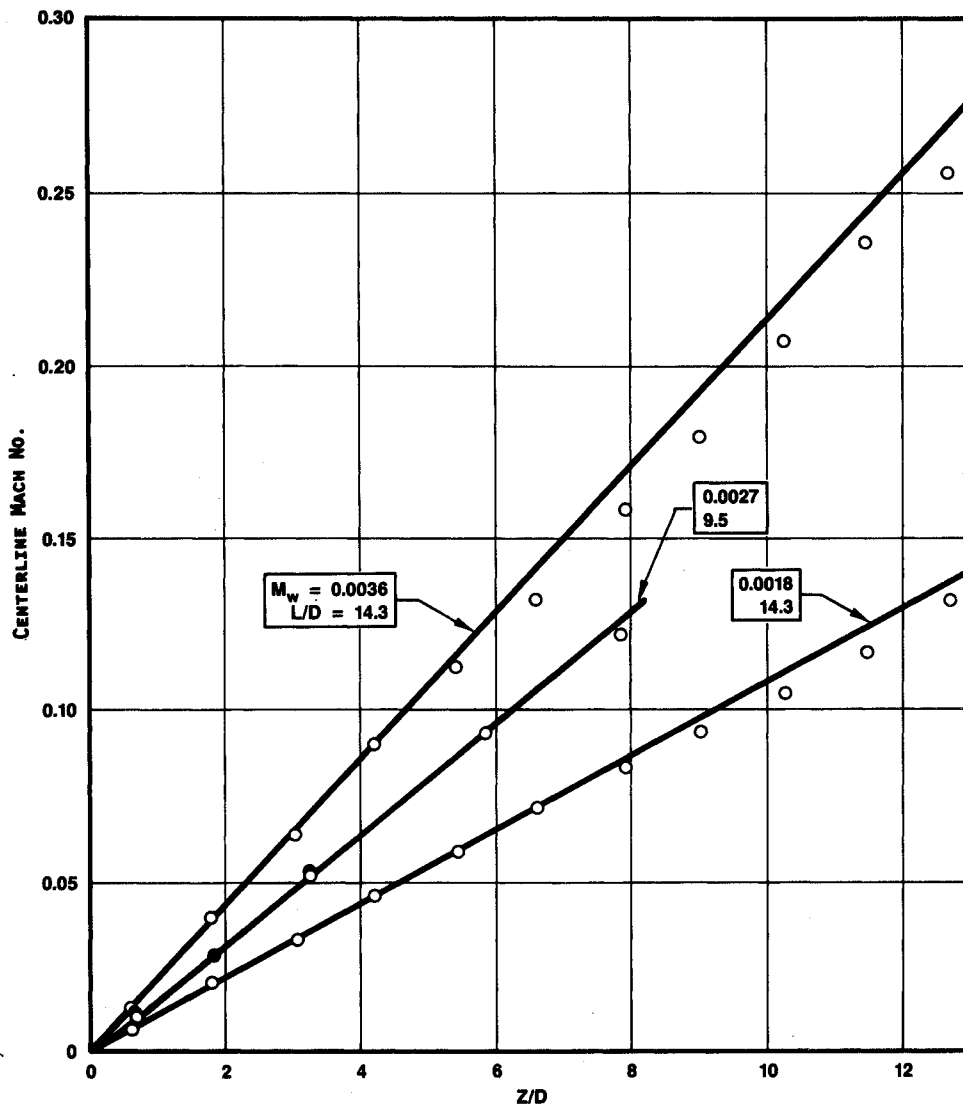$$\tau_E = \int_0^{\tau^*} \frac{\overline{u'(t)u'(t+\tau)}}{\overline{u'^2}} \, d\tau \qquad (8)$$

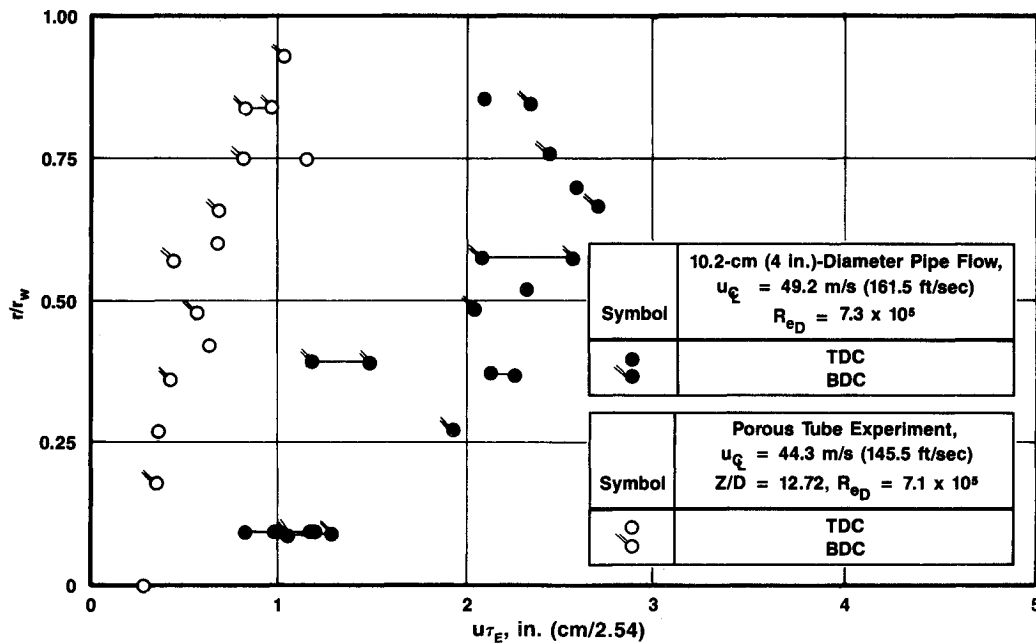Fig. 21 Centerline Mach number distributions.

Fig. 22 Turbulent integral length scales for porous tube and pipe flow.

is the Eulerian time scale, and τ^* is the first zero crossing of the u' autocorrelation. This is actually an inferred length scale using Taylor's hypothesis.[18] Comparison of the length scales in Fig. 22 reveals values in the porous tube flow that are less than half those measured in the pipe flow. This result may reflect the relatively more narrow region of intense turbulence in the injection-driven flow.

Conclusions

General observations and conclusions based on these internal flow field studies in a simulated cylindrical port rocket chamber are as follows.

1) Development of flow oscillations begins with fairly high fluctuation intensities at 0.6 diameter. The intensity decays to low levels (relative to the centerline speed) up to about 5.5 port diameters. At $Z/D = 5.5$, regular oscillations appear in the near-wall region, just prior to transition. The oscillations show frequency halving on moving away from the wall, suggestive of vortical disturbances which exhibit pairing. In the downstream turbulent regions, between 8 and 13 port diameters, the turbulent intensities have nearly constant peak and centerline values and show a slow spreading in profile shape toward the centerline. Peak intensities generally remain within a few tenths of a radius from the wall and are on the average a little higher than those in fully developed pipe flow. Peak shear stress is from 60 to 100% above the value near the wall of a pipe flow having the same centerline velocity.

2) Axial velocity profiles agree well with analytical predictions for an inviscid flow satisfying the no-slip boundary condition over most of the first 5 diameters. Further downstream, in response to moderate turbulent shear there is a gradual rounding of the profile in the midregion and some steepening near the wall.

3) A comparison of measured axial shear stress and pressure gradients shows that pressure forces acting on a fluid element are typically much greater than turbulent shear stresses. This is in qualitative agreement with the relatively gradual deviation from the inviscid solution.

4) A characteristic integral scale of the turbulence in the injection-driven flow is less than half that measured for a fully developed pipe flow.

5) Swirling flow occurs in the head-end region close to the flow centerline, at least when the axial flow is directed vertically. Peak swirl velocities are of magnitude similar to the wall-injection value.

6) Apparent buoyant effects on the flowfield have been observed in the first 3 diameters, as shown by comparative data in the horizontal and vertical positions. Estimates suggest that buoyancy could also have an influence on rocket motor chamber flow fields in some cases.

References

[1]Culick, F. E. C., "Rotational Axisymmetric Mean Flow and Damping of Acoustic Waves in Solid Propellant Rocket Motors," *AIAA Journal,* Vol. 4, No. 8, 1966, pp. 1462-1464.

[2]Dunlap, R., Willoughby, P. G., and Hermsen, R. W., "Flowfield in the Combustion Chamber of a Solid Propellant Rocket Motor," *AIAA Journal,* Vol. 12, No. 10, 1974, pp. 1440-1442.

[3]Beddini, R. A., "On the Scaling of Erosive Buring: The Threshold Condition," *Proceedings of the 15th JANNAF Combustion Meeting,* CPIA Pub. 294, Vol. II, Dec. 1978, p. 199.

[4]Beddini, R. A., "Aerothermochemical Analysis of Erosive Burning in a Laboratory Solid-Rocket Motor," *AIAA Journal,* Vol. 18, No. 11, 1980, pp. 1346-1353.

[5]Beddini, R. A., "Injection Induced Flows in Porous-Walled Ducts," *AIAA Journal,* Vol. 24, No. 11, 1986, pp. 1766-1773; see also Beddini, R. A., "Analysis of Injection-Induced Flows in Porous-Walled Ducts with Application to the Aerothermochemistry of Solid-Propellant Motors," Ph.D. Thesis, Rutgers Univ., New Brunswick, NJ, Oct. 1981.

[6]Taylor, G., "Fluid Flow Regions Bounded by Porous Surfaces," *Proceedings, Royal Society, London,* Vol. 234A, No. 1199, 1956, pp. 456-475.

[7]Dunlap, R., and Willoughby, P. G., "Cold Flow Study Test Report," United Technologies Corp., Chemical Systems Div., San Jose, CA, CSD4901-78-135, Contract F04701-77-C-0060, March 1980.

[8]Brown, R. S., Dunlap, R., Young, S. W., and Waugh, R. C., "Vortex Shedding as a Source of Acoustic Energy in Segmented Solid Rockets," *Journal of Spacecraft and Rockets,* Vol. 18, No. 7, 1981, pp. 312-319.

[9]Dunlap, R., Blackner, A. M., Brown, R. S., and Waugh, R. C., "Internal Flow Field Studies in a Simulated Longitudinally Slotted Rocket Chamber," *22nd JANNAF Combustion Meeting,* Pasadena, CA, CPIA Pub. 432, Vol. II, Oct. 1985.

[10]Dunlap, R., Blacker, A. M., Willoughby, P. G., and Jahnsen, T., "Titan IV Cold Flow Study Report," United Technologies Corp., Chemical Systems Div., San Jose, CA, CSD4001-86-89, July 1986; see

also CSD 4001-86-89, Change 1, June 1987.

[11]Brown, R. S., Blackner, A. M., Willoughby, P. G., and Dunlap, R., "Coupling Between Acoustic Velocity Oscillations and Solid Propellant Combustion," *Journal of Propulsion and Power*, Vol. 2, No. 5, 1986, pp. 428-437.

[12]Dunlap, R., et al., "Internal Flow Field Investigation," United Technologies Corp., Chemical Systems Div., Air Force Rocket Propulsion Lab., Edwards AFB, CA, Rept. AFRPL TR-86-104, March 1987.

[13]Dunlap, R., Blacker, A. M., and Jahnsen, T., "Titan Recovery Program Phase I, Task V—Internal Flow Field Studies," United Technologies Corp., Chemical Systems Div., San Jose, CA, CSD

4176-87-100, March 1987.

[14]Laufer, J., "The Structure of Turbulence in Fully Developed Pipe Flow," NACA Rept. 1174, 1954.

[15]Schlichting, H., *Boundary Layer Theory*, 1st ed., McGraw-Hill, New York, 1955.

[16]Winant, C. D., and Browand, F. K., "Vortex Pairing: The Mechanism of Turbulent Mixing-Layer Growth at Moderate Reynolds Number," *Journal of Fluid Mechanics*, Vol. 63, 1974, p. 237.

[17]Sabnis, J. S., Giebling, H. J., and McDonald, H. M., "Navier Stokes Analysis of Solid Propellant Rocket Motor Internal Flows," *Journal of Propulsion and Power*, Vol. 5, No. 6, 1989, pp. 657-664.

[18]Hinze, J. O., *Turbulence*, McGraw-Hill, New York, 1959.